Inertial effects on fibers settling in a vortical flow

Diego Lopez, Élisabeth Guazzelli

To cite this version:

Diego Lopez, Élisabeth Guazzelli. Inertial effects on fibers settling in a vortical flow. Physical Review Fluids, 2017, 2 (2), pp.024306. 10.1103/PhysRevFluids.2.024306. hal-01724974

HAL Id: hal-01724974
https://hal.science/hal-01724974v1

Submitted on 7 Mar 2018

PHYSICAL REVIEW FLUIDS **2**, 024306 (2017)

Inertial effects on fibers settling in a vortical flow

Diego Lopez[1,2,*] and Elisabeth Guazzelli[2]
[1]*Univ Lyon, INSA Lyon, CNRS, LMFA, 69100 Villeurbanne, France*
[2]*Aix Marseille Univ, CNRS, IUSTI, Marseille, France*

(Received 10 November 2016; published 28 February 2017)

Particle sedimentation under a turbulent flow is a fundamental problem that has numerous applications in natural and industrial processes. In particular, the motion of anisotropic particles yields complex dynamics whose features are not completely understood in the presence of inertia. While inertia is generally introduced through a finite particle response time, many processes involve particles with a low response time but a finite particle Reynolds number. In this case, theoretical models are rather sparse, and their validity has never been tested against controlled experiments. This work precisely proposes a careful testing of fiber sedimentation and advection models at finite particle Reynolds number against well-controlled two-dimensional experiments. We show that the slender body limit model has strong limitations at finite aspect ratio and Reynolds number, and we identify the main corrections that need to be incorporated into this basic model by expanding on the work of Khayat and Cox [J. Fluid Mech. **209**, 435 (1989)]. Additionally, we present the different models under a uniform framework, providing a simpler and clearer use. Using the validated inertial model, we show the importance of the ratio between the settling speed and the typical flow velocity for describing the fiber motion.

DOI: 10.1103/PhysRevFluids.2.024306

I. INTRODUCTION

The motion of particles in turbulent flows is of fundamental importance in several industrial and natural processes. While less documented than spherical particles, anisotropic particles are yet present in many of these flows. Common examples include pulp and paper making, ice crystals in turbulent clouds, and the transport of plankton in their complex flow environment. In many cases, sedimentation is a dominant phenomenon. The anisotropy is then adding complexity because of the coupling of the particle orientation and the center-of-mass settling velocity.

Anisotropic particles may come in many different shapes and sizes. This is particularly striking for plankton, which include bacteria, archaea, algae, protozoa, and small animals that inhabit the seas or areas of fresh water. Most of the recent studies have been nonetheless focused on the motion of elongated particles such as rodlike particles or fibers. This interest lies in great part in the availability of specific theoretical methods for slender bodies as well as in the occurrence of elongated particles in many industrial and environmental applications such as those given in the examples mentioned earlier. A key feature of these elongated particles is their tendency to adopt a preferential orientation in a turbulent flow. Tracer fibers follow Lagrangian trajectories, while their rotation depends on their orientation with respect to the local turbulent velocity gradient tensor. Conversely, fibers which are not neutrally buoyant experience preferential concentration as well as significantly different preferential alignment. An extensive review of the current literature and unresolved issues is given by Voth and Soldati [1].

The dynamics of elongated fibers settling in a turbulent flow has not been completely deciphered, as experimental studies on the dynamics of fibers under flow are rather sparse. It is only recently, in particular due to progresses in imaging techniques, that experiments on fibers were conducted in two- (2D) and three-dimensional (3D) situations [2,3]. In theses studies, the authors focused mainly

---

[*] diego.lopez@insa-lyon.fr

on the rotation rates and compared them to those predicted theoretically at low particle inertia [4]. They showed that the low-inertia prediction is very accurate in different turbulent flows provided the particles are not too long (less that seven times the Kolmogorov scale [5]). Conversely, there is an abundant literature on numerical studies with fibers and ellipsoids of different aspect ratios in turbulence. These studies have provided a better knowledge of the particle rotational dynamics, showing a preferential alignment of rods with the local vorticity and of disks perpendicular to vorticity in isotropic turbulence [6,7] as well as wall turbulence [8–10]. In most of these studies, inertia is added to the problem by considering a finite Stokes number, characterizing the response time of the particle compared to the flow time scale, while keeping a low particle Reynolds number. This condition can be achieved only for heavy particles, which raises the issue of particle settling. This feature is seldom treated with fibers, as most studies consider that the settling speed is much lower than any other velocity scale in the problem.

Particle sedimentation in an external flow has been widely studied for spherical particles, in particular in turbulence, pointing out important phenomena such as preferential sweeping [11] and an increase of the average settling speed [12,13]. These results were first anticipated considering a model cellular flow of counter-rotating vortices, initially used by Stommel [14] to study the motion of plankton in Langmuir circulation observed in lakes or oceans. In the absence of inertia, the velocity of the particle was found to be simply the sum of the local fluid velocity and its Stokes settling velocity due to gravity. Stommel showed that spherical particles could be held in permanent suspension provided the Stokes setting velocity was smaller than the maximum updraft velocity in the flow, i.e., the vortex velocity. Inertia was later included by Maxey [15,16] and many other authors [12,17,18], showing that spherical particles could not be held permanently in the vortices and settled out. This behavior has been observed in recent experiments using a cellular flow field created by electroconvection [19]. Interestingly, for Stokes number smaller than 0.1, added mass and history forces were found to be negligible, and the velocity of the particle could be still described by the sum of the fluid velocity and the particle settling velocity provided that the Stokes drag was replaced by a nonlinear drag depending of the particles Reynolds number. In the case of ellipsoids, however, Mallier and Maxey [20] considered only the Stokes regime but still found that suspension in the vortex flow was less likely, in particular as the motion of these ellipsoids was observed to be chaotic in many instances. They observed that ellipsoids settled slightly faster in this particular flow than in a quiescent fluid, which has also been pointed out by recent numerical studies in decaying isotropic turbulence [21]. The modifying effects of particle inertia on the fiber dynamics was not fully addressed by Mallier and Maxey [20]. The authors simply suggested that inertia (introduced through a finite response time) may reduce or even eliminate the chaotic motion, but no precise comparison between these predictions and experiments has been undertaken so far.

The primary objective of this paper is to present an experimental investigation of the settling of rodlike particles in a cellular flow field which mimics turbulence. Following Ref. [19], we use electroconvection to generate a 2D array of controlled vortices and track settling fibers using two cameras to measure the full fiber orientation. The fiber trajectories are compared to models which go beyond the Stokes regimes and the assumption of infinitely large aspect ratio. Statistical results regarding the mean velocity and preferential concentration or orientation are also presented. A secondary but nonetheless central objective of the paper is to present and discuss the existing theoretical models and their range of applicability. In particular, the case of finite Reynolds number will be thoroughly addressed as it can significantly impact the dynamics of settling fibers.

II. THEORETICAL MODELS

In this section, we summarize the existing models that describe the flow effect on a slender cylindrical fiber, with a special emphasis on the effect of particle inertia. Three nondimensional numbers characterize particle inertia: the Stokes number St, which compares the particle response time to the flow time scale, and two particle Reynolds numbers, one based on the local shear $\mathrm{Re}_{\dot{\gamma}}$ and another on the particle velocity relative to the flow (namely, the settling velocity) Re_{ℓ}. Considering a fiber defined by its aspect ratio $A = \ell/a \gg 1$, where ℓ is its half-length and a its radius, settling at a typical velocity W_s under a flow characterized by a length scale L_0 and a velocity scale U_0, the Stokes and Reynolds numbers can be defined as

$$\mathrm{St} = \frac{1}{3}\frac{a^2\rho_p}{\mu\epsilon}\frac{U_0}{L_0}, \quad \mathrm{Re}_{\dot{\gamma}} = \frac{\rho_f \ell^2 U_0}{\mu L_0}, \quad \mathrm{Re}_\ell = \frac{\rho_f W_s \ell}{\mu}, \tag{1}$$

where ρ_f and ρ_p are the fluid and particle densities, and μ the fluid viscosity. The parameter ϵ introduced here after Batchelor's work [22] is related to the aspect ratio through $\epsilon = 1/\ln(A)$. This small parameter for slender rods plays a key role in scaling the drag; its effect will be discussed in the next sections. The expression for the Stokes number is obtained from the particle advection equation normalized by the flow scales; a detailed derivation is provided in Appendix A. The parameters St, $\mathrm{Re}_{\dot{\gamma}}$, and Re_ℓ are related to each other through the other nondimensional quantities of the problem, such as the mass ratio, $R = \rho_p/\rho_f$, the relative size of the particles, $\lambda = \ell/L_0$, and the nondimensional reference settling velocity, $w_0 = W_s/U_0$, so that $\mathrm{St} = \mathrm{Re}_{\dot{\gamma}}\, R/A^2\epsilon = \mathrm{Re}_\ell\, \lambda R/A^2\epsilon w_0$ (disregarding the 1/3 factor).

As mentioned in the introduction, inertia is often introduced in this type of problems by considering a finite Stokes number at low particle Reynolds numbers. This condition can be achieved only if $R \gg A^2\epsilon \gg 1$ and $\ell \ll [\mu^2/(\rho_f^2 g)]^{1/3}$. The first condition cannot be satisfied in a typical liquid such as water but can be met only in a gas while the second condition imposes a limit on the particle size. This last criterion enforces that the fiber length should be smaller than about 10 μm in air, which is a strong constraint (ice crystals in clouds are generally larger than 100 μm except in very cold clouds [23]). Introducing inertia by considering a finite Stokes number but small Reynolds numbers is therefore quite restrictive and difficult to achieve in the laboratory using a regular fluid. In the present study, we decided to consider the opposite scenario where inertia is introduced through a finite settling Reynolds number Re_ℓ while keeping the Stokes number small and without any constraint on the shear Reynolds number. The expressions for the fluid drag and torque derived at low inertia must therefore be modified when the particle Reynolds number Re_ℓ is finite. This finite-Re_ℓ regime is more amenable to precise experimental examination, and this enables a direct comparison between the experiments and the theoretical models.

A. Drag force on a fiber

The forces exerted on a slender fiber under an external flow have been derived initially by Batchelor [22] and Cox [24] in the absence of inertia. Batchelor's slender body theory is valid for a body of infinite aspect ratio. When the aspect ratio is finite, the forces on the body are determined as an expansion on the small parameter $\epsilon = 1/\ln A$ [24]. Later, Khayat and Cox [25] derived the forces on a slender body for a finite Reynolds number based on the body length, using a matched asymptotic expansion on both ϵ and the Reynolds number. These models are summarized below.

We consider a cylindrical fiber as sketched in Fig. 1 submitted to an external force $\mathbf{F}$ along $\mathbf{e}_1$, translating at a velocity $\mathbf{W}$ relative to the fluid. The fiber orientation is given by a unit vector $\mathbf{p}$ that forms an angle ϕ with the force direction. Throughout the paper we will consider only the 2D problem as shown in Fig. 1.

1. Limit in the absence of inertia

In the absence of inertia, the velocity of a slender cylinder $\mathbf{W}$ is a linear function of the external force $\mathbf{F}$, so that $W_i = M_{ij}F_j$ using the Einstein summation convention. The coefficients M_{ij} characterize the mobility matrix and read

$$M_{ij} = M_\parallel p_i p_j + M_\perp(\delta_{ij} - p_i p_j), \tag{2}$$

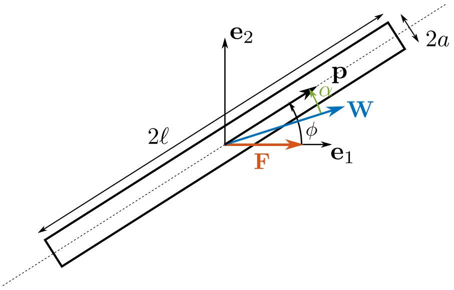

FIG. 1. Slender fiber submitted to an external force **F**, resulting in a translation at a velocity **W**.

where

$$M_{\parallel} = \frac{1}{4\pi\mu\ell\epsilon}[1 + (\ln 4 - 3/2)\epsilon + O(\epsilon^2)], \tag{3}$$

$$M_{\perp} = \frac{1}{8\pi\mu\ell\epsilon}[1 + (\ln 4 - 1/2)\epsilon + O(\epsilon^2)]. \tag{4}$$

The leading order $[M_{\parallel} = (4\pi\mu\ell\epsilon)^{-1}, M_{\perp} = (8\pi\mu\ell\epsilon)^{-1}]$ was derived initially by Batchelor [22]. In this limit it is interesting to note that $M_{\parallel} = 2M_{\perp}$, which means that the velocity of a fiber aligned with the force ($\phi = 0$) is twice that of a perpendicular fiber ($\phi = \pi/2$). In the following, this model will be referred to as the slender body limit and will be denoted M0. The first order corrections in ϵ introduced by Cox [24] account for the particle finite aspect ratio; this finite aspect ratio model will be denoted M1. These corrections result in a reduced velocity ratio compared to the slender body limit. Note that a general expression of this velocity ratio had been given for spheroidal particles by Bretherton [26].

2. *Inertial corrections*

Khayat and Cox [25] proposed a derivation of the forces exerted on a slender body under a uniform flow using a matched asymptotic expansion in both ϵ and Reynolds number, assuming that the Reynolds number $\mathrm{Re}_\ell = \rho_f W\ell/\mu$ based on the body half-length is finite, but that the Reynolds number based on the radius Re_a remains small. The resulting force on a fiber translating with a given velocity **W** is then expressed as a nonlinear function of Re_ℓ and the pitch angle denoted α in Fig. 1.

Here we are interested in the fiber velocity when submitted to an external force, as sketched in Fig. 1. In this problem we need only to determine the velocity magnitude W and the pitch angle α for a given fiber orientation ϕ. As derived in Ref. [25], one needs to solve the following system:

$$W(2 - \cos^2\alpha)[1 + F_D(\mathrm{Re}_\ell,\alpha)\epsilon] - f\cos(\phi - \alpha) = 0, \tag{5}$$

$$-W\sin\alpha\cos\alpha[1 + F_L(\mathrm{Re}_\ell,\alpha)\epsilon] + f\sin(\phi - \alpha) = 0, \tag{6}$$

where $f = F/(4\pi\mu\ell\epsilon)$, and F_D and F_L are nonlinear functions of α and Re_ℓ described in Ref. [25]; see their Eqs. (6.9) and (6.11) in the general case and their Eqs. (6.20) and (6.21) in the low Re_ℓ limit. Solving this nonlinear system gives the velocity of a fiber under an external force in the general case, but at a high computational cost as this nonlinear system must be solved at each time step.

In order to avoid this issue, we propose in this work a simpler approach for solving this problem. Since the Reynolds number corrections are computed using Oseen's solution for a line force distribution, the final problem is not reversible in time but is still linear. Assuming therefore that the linear relation $W_i = M_{ij}F_j$ still holds with a modified mobility matrix that accounts for the

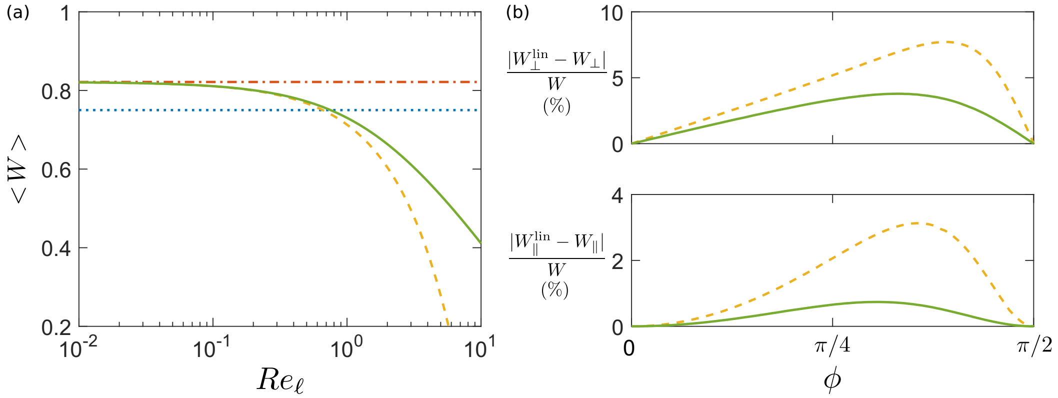

FIG. 2. Velocity of a fiber ($A = 10$) submitted to an external force, computed using the different models presented in the paper. (a) Evolution of the velocity averaged over all orientations ϕ as a function of the Reynolds number: slender body limit M0 (blue dotted line) [22], first order corrections in ϵ M1 (red dash-dotted line) [24], low-inertia corrections M2 (yellow dashed line), and general inertial corrections M3 (green line) [25]. (b) Error between linear calculation and full resolution of Ref. [25] relative to the velocity norm W at $\mathrm{Re}_\ell = 5$ as a function of the angle ϕ, for the velocity perpendicular to the force ($W_\perp$, top) and parallel to the force ($W_\parallel$, bottom): M2 (yellow dashed line) and M3 (green line).

Reynolds corrections, we can compute the mobility coefficients for $\phi = 0$ and $\phi = \pi/2$,

$$M_\parallel = \frac{1}{4\pi\mu\ell\epsilon}[1 - F_\parallel\epsilon + O(\epsilon^2)], \tag{7}$$

$$M_\perp = \frac{1}{8\pi\mu\ell\epsilon}[1 - F_\perp\epsilon + O(\epsilon^2)], \tag{8}$$

noting $F_\parallel = F_D(\mathrm{Re}_\ell,\alpha = 0)$ and $F_\perp = F_D(\mathrm{Re}_\ell,\alpha = \pi/2)$. Note that $\alpha = \phi$ in these two limit cases by symmetry. The full expressions of these functions are given in Eq. (B9) in Appendix B. However, simpler expressions emerge at low Reynolds number:

$$M_\parallel(\mathrm{Re}_\ell) = \frac{1}{4\pi\mu\ell\epsilon}\left[1 + (\ln 4 - 3/2 - \mathrm{Re}_\ell/4)\epsilon + O\left(\epsilon^2,\mathrm{Re}_\ell^2\epsilon\right)\right], \tag{9}$$

$$M_\perp(\mathrm{Re}_\ell) = \frac{1}{8\pi\mu\ell\epsilon}\left[1 + (\ln 4 - 1/2 - \mathrm{Re}_\ell/2)\epsilon + O\left(\epsilon^2,\mathrm{Re}_\ell^2\epsilon\right)\right]. \tag{10}$$

It is interesting to note that the inertial corrections affect only the $O(\epsilon)$ terms and not the leading order term. For $\mathrm{Re}_\ell = 0$, Eqs. (3) and (4) are recovered. In the following, the linear model based on the low Reynolds number expressions of Eqs. (9) and (10) will be denoted M2, whereas the linear model using the expressions of Eqs. (7) and (8) will be denoted M3.

A comparison of the different models is presented in Fig. 2, showing the velocity of a fiber ($A = 10$) under an external constant force F, computed with the different models M0, M1, M2, and M3. In Fig. 2(a), the velocity averaged over all orientations ϕ is computed as a function of the Reynolds number and normalized by f. One can readily see the influence of both finite size corrections with ϵ and inertia. For $\mathrm{Re}_\ell \geqslant 0.1$, the effect of inertial corrections becomes significant and may change the fiber motion. The validity of the linear formulation proposed in Eqs. (7) and (8) is tested in Fig. 2(b), where the errors between the linear calculation and the solution of the full problem using Eqs. (5) and (6) are shown as a function of the angle ϕ at a fixed Reynolds number ($\mathrm{Re}_\ell = 5$), relative to the norm of the fiber velocity. These errors are small and thus validate the linear model proposed here. The linear models can therefore be used for computing the inertial corrections, reducing significantly the computational cost.

B. Torque on a fiber

In this section we summarize some existing models for the flow-induced torque at zero and small but finite particle Reynolds number.

1. *Limit in the absence of inertia*

Under shear, a fiber rotates following the so-called Jeffery orbits, which are a class of closed trajectories, the choice of a particular trajectory being determined by the initial conditions [4]. The equation describing the rotation rate of the particle was derived exactly for ellipsoids [4,27], and an experimental correction for cylindrical fibers was provided in Ref. [28]. A fiber rotates fully with the rate of rotation of the flow (i.e., the rate-of-rotation tensor $\mathbf{\Omega}^\infty$) and only with a fraction β_c of the rate of extension (i.e., the rate-of-strain tensor $\mathbf{E}^\infty$) of the flow, so that the fiber orientation vector follows

$$\frac{d\mathbf{p}}{dt} = \mathbf{\Omega}^\infty \cdot \mathbf{p} + \beta_c[\mathbf{E}^\infty \cdot \mathbf{p} - (\mathbf{p} \cdot \mathbf{E}^\infty \cdot \mathbf{p})\,\mathbf{p}], \tag{11}$$

where $\beta_c = (A_c^2 - 1)/(A_c^2 + 1)$ and $A_c = 0.8A$ is the experimental correction found in Ref. [28]; this expression is the same as that for an ellipsoid, with the only change in A [29]. Note that we have followed the notations used in Eq. (3.49) in Ref. [29], where $\mathbf{\Omega}^\infty$ and $\mathbf{E}^\infty$ are tensors. The seemingly nonlinear term in Eq. (11) is here to enforce the condition that the norm of the orientation vector $\mathbf{p}$ is equal to 1. A second version of Eq. (11) can be particularly useful in 2D problems. Introducing the rotation vector $\mathbf{\Omega}_0 = \frac{1}{2}\nabla\times\mathbf{U} + \beta_c\,\mathbf{p}\times(\mathbf{E}^\infty.\,\mathbf{p})$, with $\nabla\times\mathbf{U}$ the flow vorticity [27], this can be written as $\frac{d\mathbf{p}}{dt} = \mathbf{\Omega}_0 \times \mathbf{p}$. In the present 2D problem in the $(\mathbf{e}_1,\mathbf{e}_2)$ plane, the rotation vector has only one component along the normal direction, $\mathbf{\Omega}_0 = \Omega_0\,\mathbf{e}_3$. Noting that $\mathbf{p} = \cos\phi\,\mathbf{e}_1 + \sin\phi\,\mathbf{e}_2$, the evolution of the fiber orientation is then given by a single scalar equation

$$\frac{d\phi}{dt} = \Omega_0. \tag{12}$$

2. *Inertial corrections*

When inertial effects are included, two corrections must be added to the rotation rate. The first one, denoted Ω_1, accounts for the presence of a nonzero torque under a uniform flow [25]. The total torque exerted by the fluid on the fiber is then the sum of the torque in the absence of inertia that leads to Jeffery orbits (see, e.g., Ref. [30]) and this inertial contribution. Solving the problem of a torque-free fiber, the rotation rate due to inertia under a uniform flow reads

$$\Omega_1 = -\frac{3}{4}\frac{W}{\ell}F_G(\mathrm{Re}_\ell,\alpha)\epsilon, \tag{13}$$

where F_G is a nonlinear function introduced in Ref. [25]; its general expression is given in Eq. (B10) of Appendix B. At low Reynolds number, this expression simplifies to

$$\Omega_1 = \frac{5}{16}\frac{W}{\ell}\sin(2\alpha)\,\mathrm{Re}_\ell\,\epsilon. \tag{14}$$

It is interesting to note that this correction, as that for the fluid force, acts at first order in ϵ. As an example, an inertial fiber settling in quiescent fluid no longer settles with a constant orientation as in the inertialess limit but rotates towards a stable equilibrium orientation $\alpha_{\mathrm{eq}} = \pi/2$, which corresponds to a horizontal position ($\phi_{\mathrm{eq}} = \alpha_{\mathrm{eq}}$).

A second inertial correction to the rotation rate is due to the effect of local shear [31,32]. This effect induces an additional rotation rate that scales as

$$\Omega_2 \sim \dot\gamma\,\mathrm{Re}_{\dot\gamma}\,\epsilon \quad \text{with} \quad \mathrm{Re}_{\dot\gamma} = \frac{\rho_f\dot\gamma\ell^2}{\mu}, \tag{15}$$

where $\dot{\gamma}$ is the shear rate. The total rotation rate should be in the general case a superposition of the inertialess rotation rate Ω_0 and these two additional effects. In the next section, we consider these models in the framework of our present study and identify the different corrections that may significantly change the fiber dynamics.

C. Application to the present study

1. *Nondimensional parameters and orders of magnitude*

The different expansions summarized above imply two key parameters. The first one denoted ϵ is related to the high slenderness of the fiber. However, the logarithmic dependence of ϵ on the aspect ratio is very restrictive as $\epsilon \sim 0.1$ corresponds to an extremely slender body ($A \sim 10^4$). This is almost never achieved experimentally, where the typical aspect ratios range from $A = 10$ ($\epsilon \approx 0.4$) to $A = 100$ ($\epsilon \approx 0.2$). We therefore expect the first order corrections in ϵ to be significant in our problem, as shown in Fig. 2. The second parameter is the Reynolds number based on the fiber half-length, which has no specified value, provided the Reynolds number based on the radius Re_a is small. However, it is important to note that the two Reynolds numbers are related through $\mathrm{Re}_\ell = A\mathrm{Re}_a$, so that Re_ℓ cannot take arbitrary values independently of the aspect ratio. These orders of magnitude must be considered carefully, as higher order terms in $O(\epsilon^2)$ can possibly be larger than $O(\mathrm{Re}_\ell\epsilon)$ terms.

In the present work, we will consider a fiber settling in a cellular flow. The reference settling velocity is taken as that given by the leading order expression for the sedimentation velocity of a fiber perpendicular to gravity, $W_s = (\rho_p - \rho_f)a^2 g/(4\mu\epsilon)$. This yields a nondimensional reference velocity $w_0 \in [0.5; 2]$ in all experiments. Among the different dimensionless parameters that characterize the problem, only the fiber Reynolds number $\mathrm{Re}_\ell = \rho_f W_s \ell/\mu$ will play a significant role, ranging from 0.1 to 10. The flow Reynolds number Re will modify the cellular flow, and its effect will be discussed in the next section. The maximum Stokes number is 10^{-3}, the mass ratio R is kept slightly larger than 1, and the relative size λ is lower than 0.25. The effect of the aspect ratio A (from 10 to 30) is mainly observable through the particle Reynolds number and not through ϵ, which does not vary significantly for these aspect ratios ($\epsilon \in [0.3; 0.4]$).

The different corrections to the rotation rate can now be compared in terms of characteristic time scales. We call t_0 the time scale associated with the zero-Reynolds number rotation rate Ω_0. Noting t_1 the time scale associated with the rotation rate Ω_1 induced by inertial effects in a uniform flow and t_2 the correction to the shear contribution associated with the rotation rate Ω_2, we have

$$\frac{t_1}{t_0} = \frac{\lambda}{\epsilon\, w_0\, \mathrm{Re}_\ell}, \quad \frac{t_2}{t_1} = \left(\frac{w_0}{\lambda}\right)^2. \tag{16}$$

Since $t_2/t_1 > 10$ in the present study, the corrections due to inertia on the shear-induced rotation rate Ω_2 are negligible compared to those associated with Ω_1. Conversely, since $t_1/t_0 \in [0.1; 10]$, the correction due to inertial effects under a uniform flow can occur on a similar time scale as Ω_0 and must therefore be taken into account.

2. *Equations of the problem*

Similarly to what has been shown for spheres [14,19], we consider that, at low Stokes number, the fiber velocity $\mathbf{V}$ is given by the superimposition of the external flow $\mathbf{U}$ and the settling speed in a fluid at rest $\mathbf{W}$. We consider in the following a fiber settling in the (y,z) plane, z being the direction of gravity, oriented upwards ($\mathbf{g} = -g\mathbf{e}_z$). The fiber is described by its orientation vector $\mathbf{p}$, which forms an angle θ with the horizontal axis $\mathbf{e}_y$, so that $\mathbf{p} = \cos\theta\,\mathbf{e}_y + \sin\theta\,\mathbf{e}_z$ ($\theta \in [-\pi/2; \pi/2]$). Considering the general notations of Fig. 1, we have now $\mathbf{e}_1 = -\mathbf{e}_z$ and $\phi = \theta + \pi/2$ [see Fig. 3(c)].

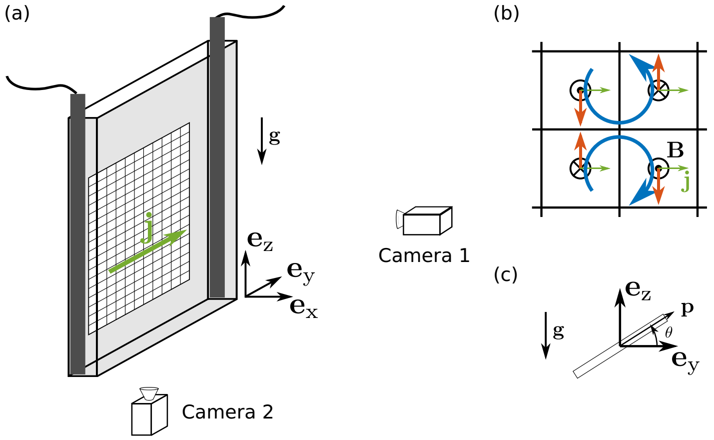

FIG. 3. (a) Experimental setup: tank, cameras for velocimetry, and fiber tracking. The two carbon electrodes are represented in black, creating an electric current **j**. The magnetic field is generated by a checkerboard of magnets place behind the back wall of the tank. (b) Sketch of the flow generation in the (y,z) plane: in the presence of a magnetic field **B**, the electric current (green arrows) gives rise to an electromagnetic force in the fluid (red arrows), resulting in a flow of counter-rotating vortices (blue arrows). (c) Parameters with definition of the axes for the settling fiber.

The nondimensional fiber velocity and rotation rate read

$$\mathbf{v} = \mathbf{u} + \mathbf{w}, \tag{17}$$

$$\dot{\theta} = \omega_0 + \tilde{\omega}(w,\lambda,\alpha,\epsilon,\mathrm{Re}_\ell), \tag{18}$$

where lower-case letters denote nondimensional quantities. Here

$$w_y = -w_0 \cos\theta \sin\theta \, G_y(\epsilon,\mathrm{Re}_\ell), \tag{19}$$

$$w_z = -w_0(1 + \sin^2\theta)\, G_z(\epsilon,\mathrm{Re}_\ell,\theta). \tag{20}$$

with $w_0 = W_s/U_0$, $\omega_0 = \Omega_0/(U_0/L_0)$, w is the norm of the nondimensional slip velocity (equal to the settling velocity), and α is the fiber angle of attack relative to the fluid. The functions G_y, G_z, and $\tilde{\omega}$ depend on the different models used. In the following, we will compare the experimental results to the computations using four different models: (1) slender body limit (M0), (2) first order corrections on ϵ without inertia (M1), (3) first order corrections on ϵ and inertial corrections in the low Reynolds number limit (M2), and (4) first order corrections on ϵ and inertial corrections in the general case (M3). The detailed expressions of G_y, G_z, and $\tilde{\omega}$ are given in Appendix B for each model. It should be stressed that for models M2 and M3 the rotational velocity is that given in Ref. [25] whereas the translational velocity is a linear version of their formulation involving a mobility matrix as defined in Eq. (2).

III. EXPERIMENTAL SETUP AND METHOD

The experimental setup is the same as that of Ref. [19] and is shown in Fig. 3. It consists of a tank made of Plexiglas® (of 50 cm height, 38 cm width, and 4 cm depth) filled with an aqueous mixture of citric acid and Ucon Oil®. The vortical flow is activated by electromagnetic forcing, i.e., an array of Laplace forces $\mathbf{j}\times\mathbf{B}$ where $\mathbf{j}$ is the electrical current density and $\mathbf{B}$ is the magnetic field. The magnetic field is produced by a checkerboard of permanent square magnets (NdFeB, $\mathrm{Br} \approx 1.3$ T, 2×2 cm^2) placed against the back wall of the tank of 2 mm thickness. The electrical current is driven between two carbon electrodes placed on opposite sides of the tank. Since the electrical current

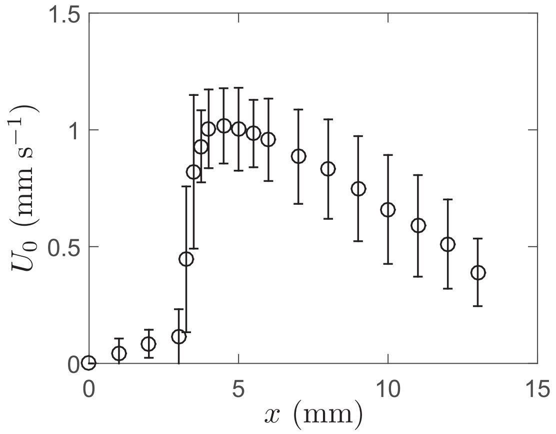

FIG. 4. Evolution of the vortex intensity U_0 as a function of the distance to the back wall for a fluid Reynolds number $\mathrm{Re} = 0.2$.

density j is uniform, the spatial distribution of the electromagnetic forcing is determined by the position and size of the magnets, see Fig. 3(b).

The flow characterization is performed by particle image velocimetry (PIV) using the Matlab$^{\mathrm{TM}}$PIV software DPIVsoft [33]. The fluid is seeded with hollow particles used as fluid tracers (Dantec Measurement Technology, with diameter $\approx$15 μm and density $\approx$1.4 g cm^{-3}). The tank is illuminated by a green laser sheet (Laser Lasever LSR-NL, 532 nm, 500 mW) aligned with the vertical plane (y,z). Two digital cameras (Pike F210B and Prosilica GX1910, Allied Vision Technologies, 1920$\times$1080 pixels^2) are used, one placed at a right angle to the light sheet in front of the tank, and the other placed below the tank at a right angle with the horizontal plane. For the PIV measurements, the camera is focused on the illuminated particles, which scatter the light. Two images separated in time by typically 1/31 to 4/31 s are then recorded and processed using cross-correlations to find the velocity-vector map of the flow field. The spatial resolution of the measurement is given by the correlation window size (from 1/10 to 1/5 of the vortex size), while the flow-velocity resolution is given by the time separation between the two images.

The flow generated by this setup is a periodic flow of counter-rotating vortices in the (y,z) plane, the intensity of which reaches a maximum at about $x \approx 5$ mm and then decays rapidly; see Fig. 4. At $x \approx 5$ mm, the flow component normal to the back wall is negligible compared to the vortex intensity, resulting in a quasi-2D flow. It is interesting to note that this flow is very similar to the Taylor-Green cellular flow described by the stream function

$$\psi = \frac{U_0 L_0}{\pi} \sin\left(\frac{\pi y}{L_0}\right) \sin\left(\frac{\pi z}{L_0}\right), \tag{21}$$

for the typical flow Reynolds numbers considered in the experiments [19]. At low fluid Reynolds number Re the flow measured by PIV and that predicted by the Taylor-Green model are equivalent, the computations are thus performed using the Taylor-Green vortex flow. At larger Re we use an interpolation on the PIV measured flow since the cellular flow progressively departs from the Taylor-Green model. This will be discussed in Sec. IV A.

Fibers are dropped from the top of the tank and settle through the cellular flow. The fibers are made of nylon (fishing line) of diameter $2a = 280 \pm 5$ μm and density $\rho_p = 1.15 \pm 0.01$ g cm^{-3}. Three different half-lengths ℓ were used, $\ell = 1.6$, 3.2, and 4.8 mm, resulting in three typical aspect ratios $A = 11.5$, 23, and 34.5. The fiber are immersed for a day before the experiment in order to reduce the entrapment of air bubbles on the particles. This process did not alter their properties. The fibers are then dropped one by one through a small tube located at $x = 5$ mm, and followed

TABLE I. Dimensionless numbers for the different combinations of particles and fluids used in the experiments.

Experiment	1A	1C	2A	2B	2C
Fluid	1	1	2	2	2
A	11.5	34.5	11.5	23	34.5
Re_ℓ	0.09	0.39	2.0	5.1	8.6
w_0	[0.35; 0.85]	[0.43; 0.93]	[0.66; 1.3]	[0.91; 1.4]	[0.97; 1.8]
St	6.6×10^{-5}	1.4×10^{-4}	8.7×10^{-4}	1.1×10^{-3}	1.2×10^{-3}
Re	∼2	∼2	∼25	∼25	∼25

using particle tracking with the two cameras synchronized by an external trigger. This provided the capture of the full trajectory and orientation of each fiber. The sedimentation experiments were conducted with two different fluids, one for the low inertia case (fluid 1: $\rho_f = 1.092\,\mathrm{g\,cm^{-3}}$ and $\mu = 11.2$ mPa s), and a second for the inertial case (fluid 2: $\rho_f = 1.108\,\mathrm{g\,cm^{-3}}$ and $\mu = 2.0$ mPa s). The dimensionless numbers corresponding to the different experiments are given in Table I.

Due to particle anisotropy, any perturbation orienting the fiber out of the (y,z) plane would result in a fully 3D trajectory. This was limited by the dropping device but could not be completely avoided, as can be seen in Fig. 5. In this figure, three typical experimental trajectories of settling fibers in

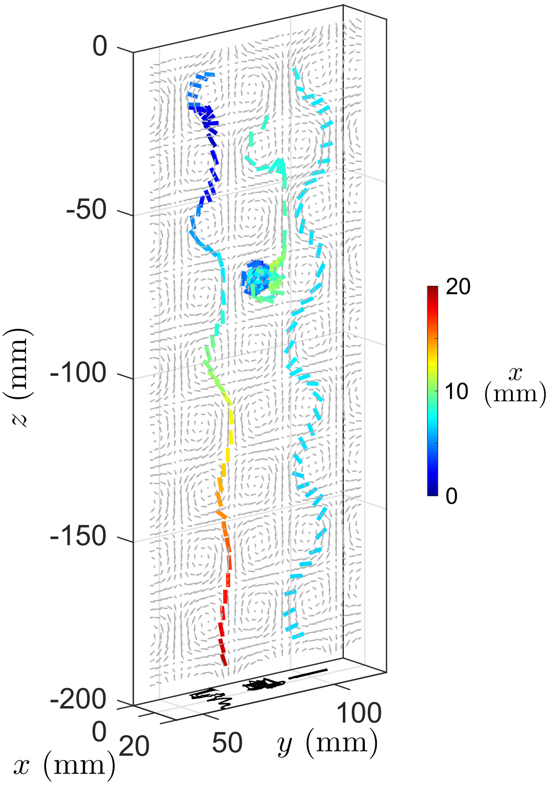

FIG. 5. Three typical trajectories of fibers settling in a cellular flow obtained for $A = 11.5$, $\mathrm{Re}_\ell = 0.1$. The colors correspond to the distance to the back wall, and the trajectories projected in the horizontal plane are shown at the bottom. Whereas the first two fibers on the left side experience a 3D trajectory, the third fiber on the right side follows a 2D trajectory and is therefore suitable for comparison with 2D flow models.

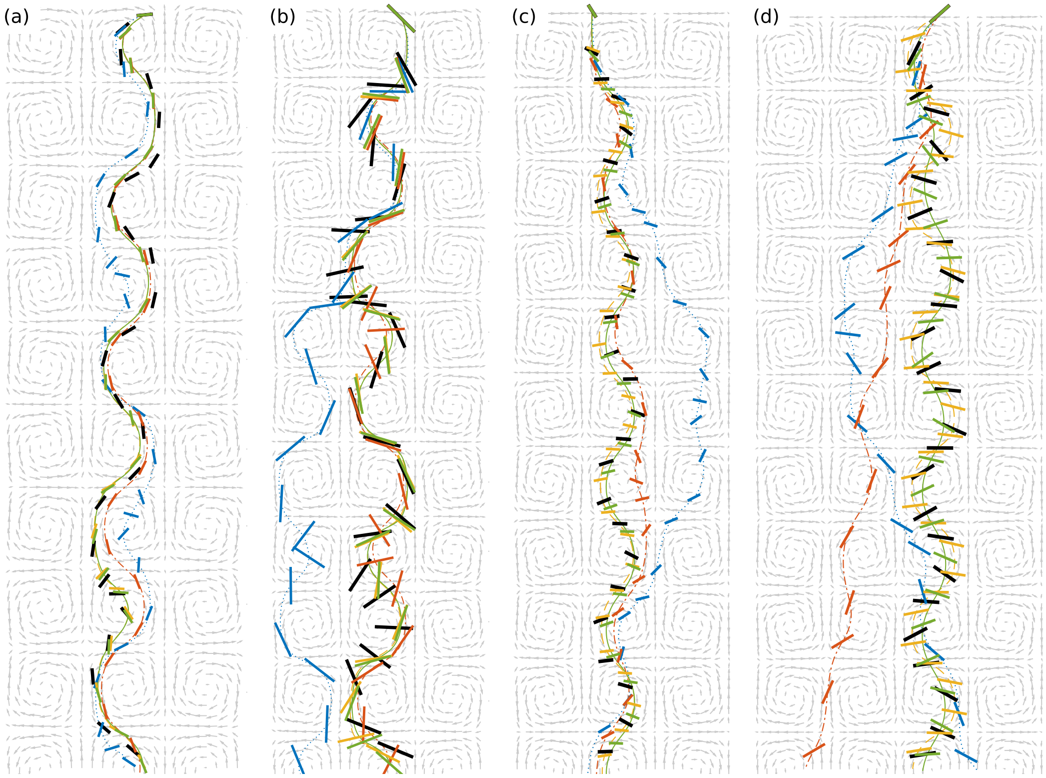

FIG. 6. Experimental trajectories (black) and modeled trajectories using the four models (M0: blue, dotted line; M1: red, dash-dotted line; M2: yellow, dashed line; M3: green, solid line), for four values of the Reynolds number: (a) $\mathrm{Re}_\ell = 0.1$ (case 1A, $w_0 = 0.60$, time step between two successive positions $\Delta t = 7.5$ s), (b) $\mathrm{Re}_\ell = 0.4$ (1C, $w_0 = 0.48$, $\Delta t = 5.8$ s), (c) $\mathrm{Re}_\ell = 2.0$ (2A, $w_0 = 1.1$, $\Delta t = 2.8$ s), (d) $\mathrm{Re}_\ell = 5.1$ (2B, $w_0 = 1.4$, $\Delta t = 3.0$ s).

the cellular flow are shown. The color coding (color online) corresponds to the distance to the back wall, which is also visualized by the projected trajectories at the bottom of the plot. The first two fibers (on the left side) follow a 3D trajectory, whereas the third fiber (on the right side) stays in a fixed (y,z) plane. Since we do not have a full description of the flow generated in the tank but only a 2D one, only 2D trajectories were selected from all experiments and used for comparison with the theoretical models (i.e., the third fiber in Fig. 5), which represented approximately 50% of the total number of fibers tested.

IV. COMPARISON OF THE MODELS WITH EXPERIMENTS

A. Individual trajectories

In this first section we are interested in comparing the four models presented above with individual experimental trajectories. Figure 6 shows four different experiments at increasing Reynolds numbers $\mathrm{Re}_\ell = 0.1$ (case 1A), 0.4 (1C), 2.0 (2A), and $\mathrm{Re}_\ell = 5.1$ (2B), compared to the theoretical predictions. The experimental trajectories are represented in black by superimposing the fiber position at different times, and each color (color online) corresponds to a different model (M0: blue, M1: red, M2: yellow, M3: green). The trajectory of the center of mass is also represented with the same line style as in Fig. 2. These simulations were based on the Taylor-Green flow model. The experimental trajectories show that fibers tend to settle along the downstream flow regions in the periphery of the vortices. As

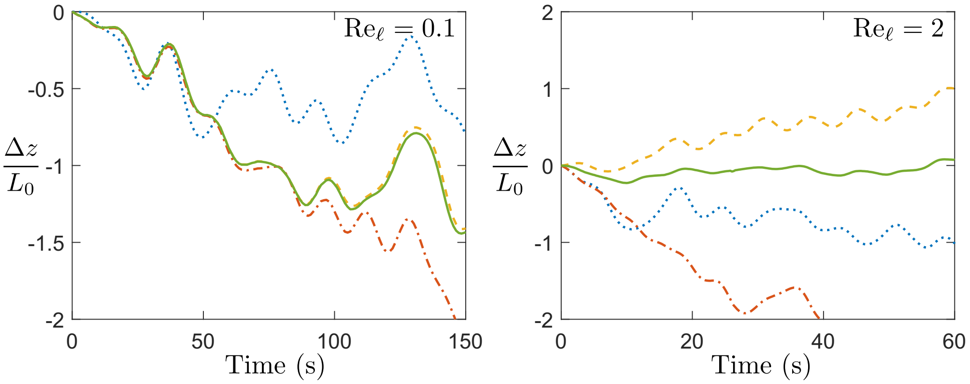

FIG. 7. Time evolution of the error in altitude between numerical simulations and experiments $\Delta z = z_{\mathrm{num}} - z_{\mathrm{exp}}$ normalized by the flow length scale for all models (M0: blue, dotted line; M1: red, dash-dotted line; M2: yellow, dashed line; M3: green, solid line), for $\mathrm{Re}_\ell = 0.1$ (case 1A, $w_0 = 0.60$) and $\mathrm{Re}_\ell = 2.0$ (2A, $w_0 = 1.1$).

inertia increases, this effect seems to be reduced. One can also observe that at large inertia [Figs. 6(c) and 6(d)] fibers settle mostly horizontally, whereas they settle with a seemingly isotropic orientation at low inertia.

Starting with the same initial conditions as in the experiments, the theoretical trajectories are computed using the four different models. At low Re_ℓ [Figs. 6(a) and 6(b)], we see that all models are in good agreement with experimental data except for the slender body limit M0. The finite aspect ratio corrections are predominant, in particular for $A = 11.5$ [Fig. 6(a)]. As the aspect ratio increases this effect should be reduced. This is actually observed in Fig. 6(b) where model M0 predicts a consistent trajectory during three vortices, before diverging from the experimental data. This first result shows the important role played by the finite aspect ratio corrections for capturing individual trajectories. In this low inertia cases, models M1, M2, and M3 predict similar trajectories during the first three periodic cells (six vortices), but then the inertialess model (M1) diverges slightly from the experimental results, whereas the two models accounting for both finite size effect and inertia (M2 and M3) are in excellent agreement with the experimental trajectory. In this case, M2 and M3 give almost identical results, as M2 is simply a low Reynolds number formulation of M3. Note that when the fibers are longer [Fig. 6(b)], they become very sensitive to the particular flow used here, as the particle goes through a saddle point after each cell, and the direction followed is strongly dependent on any type of perturbation. This limits the models accuracy, as the predictions of models M2 and M3 eventually diverge from the experimental trajectory. As the Reynolds number becomes larger than 1 [Figs. 6(c) and 6(d)] these trends tend to be more pronounced, and only the trajectories predicted by models M2 and M3 are consistent with the experiments.

The comparison between the different models and the experiments can be also analyzed through the instantaneous error between the altitude z_{num} predicted by the models and the experimental one z_{exp}. This is shown in Fig. 7 for the cases at $\mathrm{Re}_\ell = 0.1$ and $\mathrm{Re}_\ell = 2.0$ of Fig. 6. At low particle Reynolds number [Fig. 7(a)] all models predict a faster settling rate without clear distinctive trends between different models. This inaccuracy is actually related to the experimental difficulties at low inertia. Here the typical settling velocity is of 1 $\mathrm{mm\,s^{-1}}$, so that the particles are very sensitive to any type of perturbation such as the vortex shape and velocity fluctuations or thermal convection in the tank over these long times. Note that the typical relative error in settling velocity ranges from 15% to 30% in these cases; this will be further discussed in Sec. IV B 2. As the particle inertia increases [Fig. 7(b)] this systematic error vanishes, and clear trends emerge between the different models, showing that only model M3 captures the instantaneous settling rate accurately.

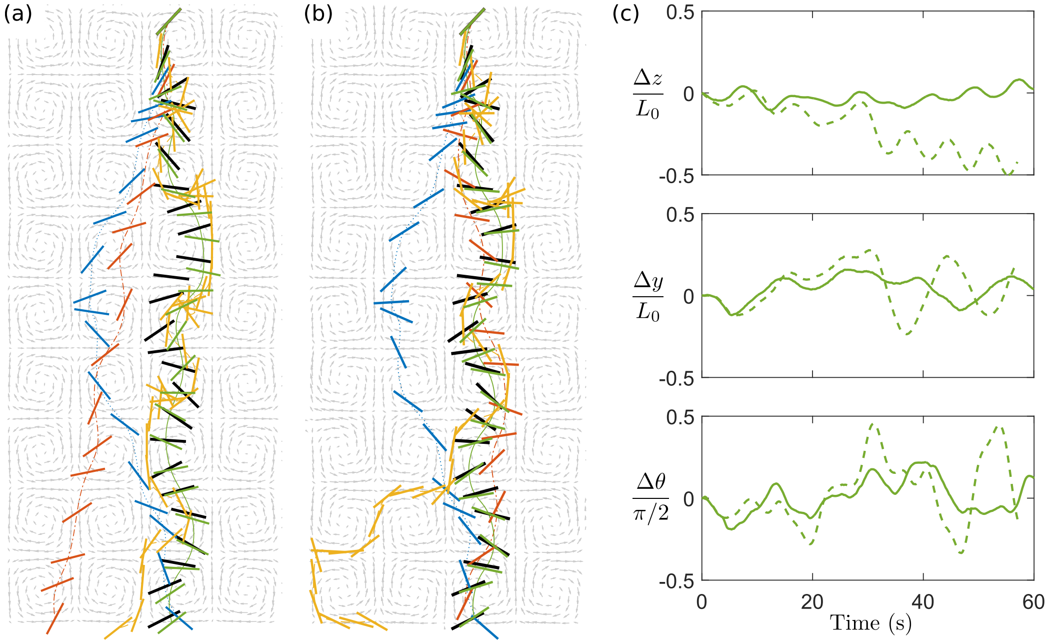

FIG. 8. Flow model effect at large Reynolds number $\mathrm{Re}_\ell = 8.6$ (case 2C): Experimental and modeled trajectories as in Fig. 6 for $A = 34.5$, $w_0 = 1.5$ and $\Delta t = 2.4$ s, using (a) Taylor-Green model flow Eq. (21) and (b) interpolation on the PIV measurements. (c) Time evolution of the errors $\Delta z = z_{\mathrm{num}} - z_{\mathrm{exp}}$, $\Delta y = y_{\mathrm{num}} - y_{\mathrm{exp}}$, and $\Delta\theta = \theta_{\mathrm{num}} - \theta_{\mathrm{exp}}$ between M3 model predictions and the experiment using Taylor-Green flow (dashed line) and PIV measurements (solid line).

The experiments at large particle Reynolds number ($\mathrm{Re}_\ell \geqslant 2$) are conducted with the low viscosity fluid (fluid 2), resulting in a large fluid Reynolds number ($\mathrm{Re} \approx 25$; see Table I). In this case, the actual flow differs from the Taylor-Green model. In order to address this issue, the same simulations were performed using first the Taylor-Green Vortex (TGV) flow, and then the flow measured by PIV. In the latter a standard 2D cubic interpolation was used for computing the flow and corresponding gradients at the fiber location. The comparison between these two methods is shown in Fig. 8 for a fiber settling at $\mathrm{Re}_\ell = 8.6$ (case 2C). In Figs. 8(a) and 8(b), the trajectories computed on the TGV flow and PIV flow, respectively, are represented as in Fig. 6, showing the significant differences between the theoretical models as well as the impact of the flow model used in the computations. For this high Reynolds number case the differences between models are even more pronounced, and discrepancies between models M2 and M3 are clearly visible. In this regime only the model accounting for both finite size effect and inertia in the general case (M3) provides accurate predictions, while the other models fail to predict consistent trajectories. Figure 8(c) shows the errors between numerical simulations and experiments in z, y, and θ the angle with respect to the horizontal axis as a function of time, comparing model M3 computed on the TGV flow (dashed line) and PIV flow (solid line) with the experimental data. We see that the predictions based on the PIV flow are in excellent agreement with the experiments, whereas the TGV model leads to some discrepancies, in particular a slightly higher settling rate.

The comparison between the four models and experimental trajectories showed the importance of finite size and inertial corrections for capturing individual trajectories. In particular at low Reynolds number finite size corrections have a significant impact on the trajectories. Inertial corrections play a small role for $\mathrm{Re}_\ell < 1$ but are of primary importance for $\mathrm{Re}_\ell \geqslant 1$ and must therefore be accounted for. In the next section we turn to statistical results for a quantitative comparison between the different models and the experiments.

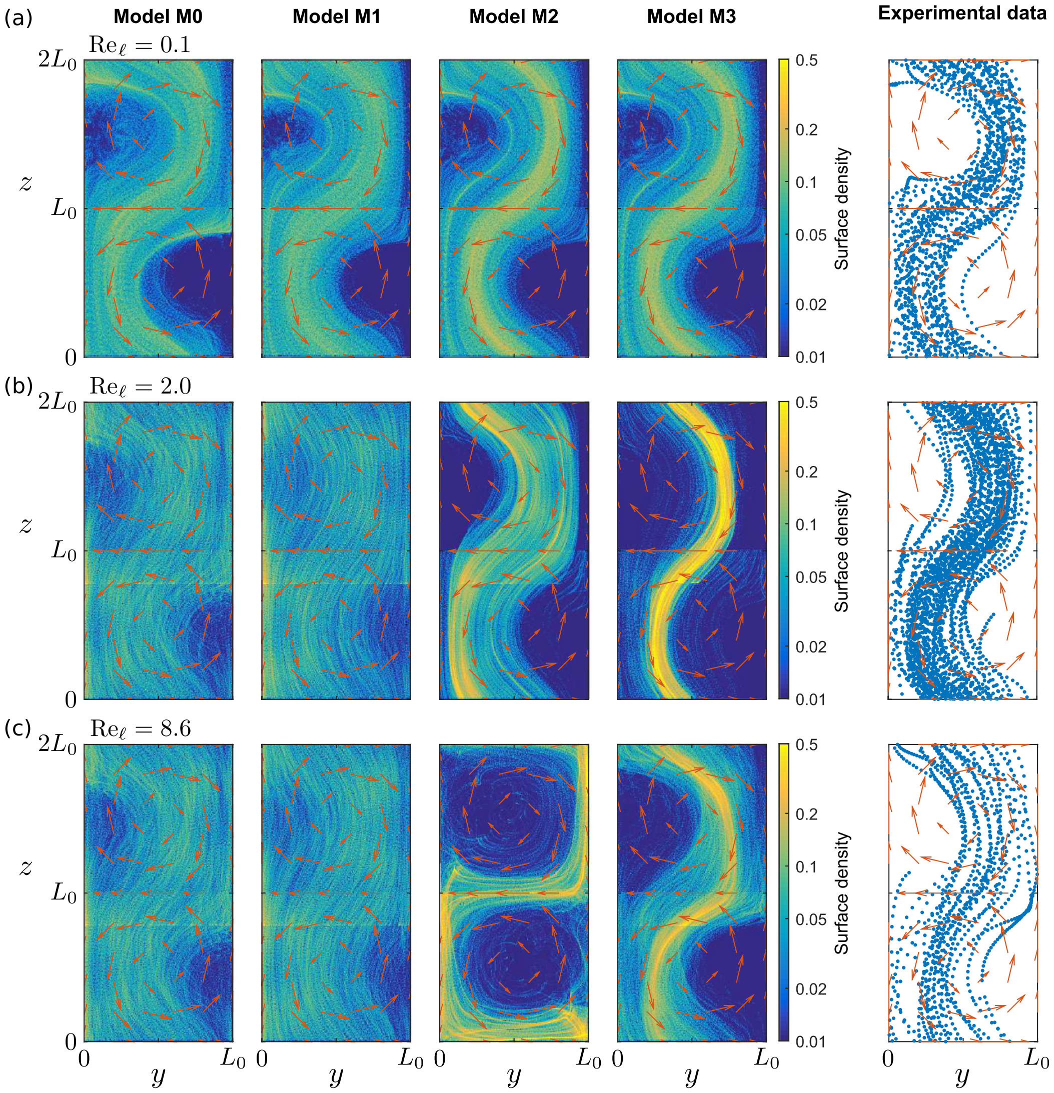

FIG. 9. Preferential concentration of fibers: particle surface density in a cell obtained by projection of each position. The four models are compared to the experimental data for (a) $\mathrm{Re}_\ell = 0.1$ ($w_0 = 0.5$), (b) $\mathrm{Re}_\ell = 2.0$ ($w_0 = 1$), and (c) $\mathrm{Re}_\ell = 8.6$ ($w_0 = 1$).

B. Statistical results

We are interested now in comparing the predictions of the different models with our experimental results on preferential concentration and orientation as well as the average settling speed. Consistently with what was observed on individual trajectories, the results presented for low inertia ($\mathrm{Re}_\ell \leqslant 1$) are computed using the Taylor-Green model flow, whereas for $\mathrm{Re}_\ell \geqslant 1$ the calculations are performed by interpolation on the PIV measurements.

1. Preferential concentration and orientation

An important feature observed for particles in an external flow is the existence of preferred trajectories rather than a random sampling of the flow. Figure 9 shows these preferred regions

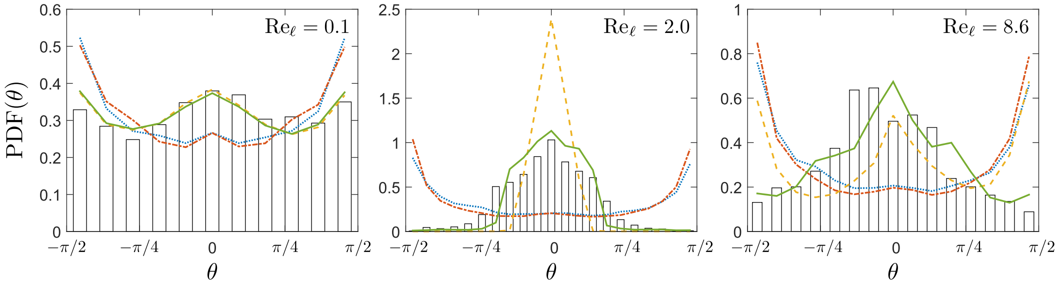

FIG. 10. Probability density function of the angle with the horizontal axis θ for three values of the particle Reynolds number $\mathrm{Re}_\ell = 0.1$, $\mathrm{Re}_\ell = 2.0$, and $\mathrm{Re}_\ell = 8.6$: experiments (bars) and numerical results (M0: blue dotted line, M1: red dash-dotted line, M2: yellow dashed line, M3: green line).

predicted by the four different models and compared to the experimental measures for three typical values of the particle Reynolds number: $\mathrm{Re}_\ell = 0.1$ (1A), 2.0 (2A), and 8.6 (2C). The simulations are run over 1000 trajectories with random initial conditions in a periodic cell, and over 15 periodic cells vertically for simulations at low Re_ℓ (TGV flow) and 11 periodic cells at large Re_ℓ. The resulting trajectories are then projected in one periodic cell ($[0; L_0]$ on y and $[0; 2L_0]$ on z), and the surface density is shown in color level with a logarithmic scale.

As observed previously on individual trajectories, the experimental data show that fibers settle preferentially along the downflow regions. As inertia increases, this effect weakens but is still observed. This effect is well captured by all four models at low inertia. The two models accounting for inertia (M2 and M3) predict a narrower region of preferential concentration, which seems to be more accurate than the broad region predicted by the inertialess models M0 and M1. As inertia increases, the differences between models become significant, and inertial models show a much better agreement with the experiments. At large inertia [Fig. 9(c)] only the complete model accounting for finite size effects and inertial corrections in the general case (M3) captures well the region sampled by the settling fibers.

Considering now the probability density functions of the orientation θ shown in Fig. 10 at the same three Re_ℓ, we see that the experimental distribution is almost isotropic at low inertia, with two slightly dominant orientations at $\theta = 0$ and $\theta = \pm\pi/2$, corresponding, respectively, to horizontal and vertical orientations. However, as inertia increases, the distribution becomes clearly anisotropic with a strong peak at $\theta = 0$, showing that fibers settle mainly horizontally. This corresponds to the stable orientation of a fiber settling at finite inertia in a quiescent fluid. The experimental orientation distributions are well captured only by the models accounting for inertial effects, even at low Reynolds number. Again, as inertia increases, only M3 provides accurate predictions compared to the experiments. In particular, models M0, M1, and M2 predict a peak at $\theta = \pm\pi/2$ (corresponding to a vertical fiber), which is inconsistent with the distributions observed experimentally.

2. Settling rate

Predicting the average settling speed is particularly important in many ecological and industrial applications. We therefore perform a last comparison between the different models by computing the effective settling velocity. Figure 11 shows the settling velocity across a cell averaged along all cells $\langle V_z \rangle$ and normalized by the reference settling speed W_s. The experimental results show that the effective settling velocity decreases as w_0 increases, i.e., as the flow velocity decreases. At low w_0 and low particle inertia, settling is strongly enhanced by the vortices, as fibers settle more than two times faster than the reference velocity W_s. At larger w_0 and particle inertia, we observe that the ratio $\langle V_z \rangle / W_s$ tends to 1, corresponding to the settling velocity of a horizontal fiber without any external flow. This is consistent with the previous observations on the preferred orientation and suggests that in such regime the flow does not affect significantly the fiber dynamics.

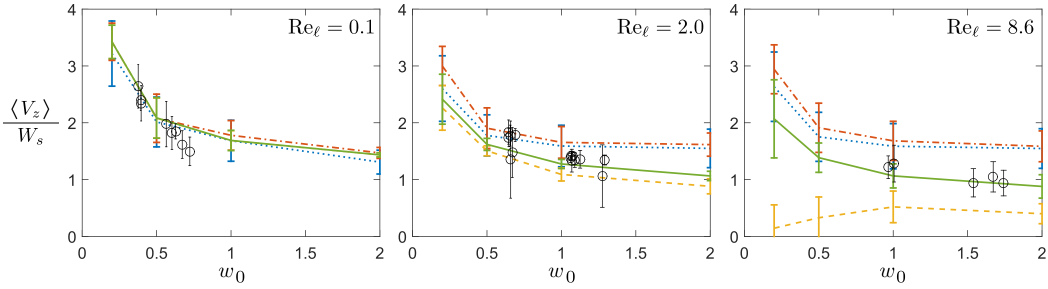

FIG. 11. Effective settling velocity averaged over each cell $\langle V_z \rangle$ normalized by the reference settling speed W_s, as a function of w_0, for three values of the particle Reynolds number $\mathrm{Re}_\ell = 0.1$, $\mathrm{Re}_\ell = 2.0$, and $\mathrm{Re}_\ell = 8.6$: experiments (black circles) and numerical results (M0: blue dotted line, M1: red dash-dotted line, M2: yellow dashed line, M3: green line).

A first observation when comparing with the different models is that at low inertia, all models give almost identical predictions. This is even more surprising as the settling velocity is correctly computed using the inertialess slender body limit (M0). The experimental results agree well with these calculation, especially considering that the experimental trajectories are generally short (8–10 vortices) and the resulting statistics hardly converged. When inertia increases, the differences between models become significant, with a predicted settling speed that can be changed by a factor two to four between M2 and M0. Once again, only the complete model M3 is in good agreement with the experiments in all regimes.

V. DISCUSSION AND CONCLUSION

In this work we studied the effect of inertia on fiber sedimentation in a cellular flow made of counter-rotating vortices. Using 2D experiments and numerical simulations, we compared different theoretical models and identified the importance of finite size and inertial corrections in theoretical predictions.

A first important result that was highlighted by considering individual trajectories is that the slender body limit model (M0) is never able to predict consistent trajectories, for aspect ratios up to 34.5, which are representative of most natural and industrial slender objects. Accounting for first order corrections in the aspect ratio—through the parameter ϵ in models M1, M2, and M3—is therefore crucial for modeling individual trajectories. The comparison of individual trajectories also suggests that inertial corrections need to be included only above a particle Reynolds number of order 1. The low inertia approximation of model M2 appears to be valid up to $\mathrm{Re}_\ell \sim 5$ for the trajectories but underestimates the instantaneous settling speed. Only the full model M3 captures well the trajectories and instantaneous settling rate above $\mathrm{Re}_\ell = 1$.

We then turned to the concentration of fibers in preferential regions, also referred to as preferential sweeping. For describing this effect, all models (including M0) proved to be equivalent at low particle Reynolds number $\mathrm{Re}_\ell = O(0.1)$. As inertia increases, discrepancies between the different models become significant, and only inertial models capture correctly the region explored by the fibers. In the experiments, only the case $w_0 = O(1)$ was studied because it presented the most interesting phenomenology. We can explore the issue of preferential sweeping further by considering the effect of the reference settling speed w_0. Figure 12 presents the particle density in a cell for three values of the reference velocity $w_0 = W_s/U_0 = 0.1$, 1, and 10, for particle Reynolds numbers of $\mathrm{Re}_\ell = 10^{-2}$ and 10; these results were computed using model M3 on the Taylor-Green model flow. At low w_0 the fibers converge to a narrow region along the downward flow at the periphery of the vortices. It is important to note that contrary to what has been observed for spheres [14,19], this effect is independent of the Reynolds number and occurs even in the absence of inertia ($\mathrm{Re}_\ell = 10^{-2}$), resulting from the rotational dynamics and the anisotropic drag.

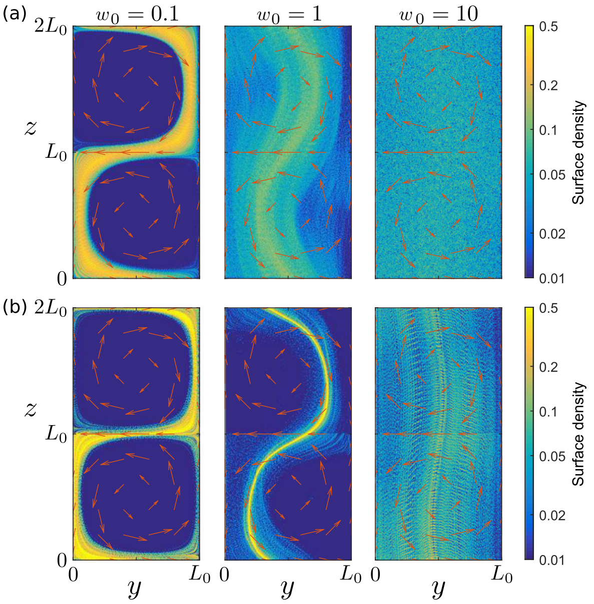

FIG. 12. Effect of the nondimensional settling velocity w_0 on preferential concentration of fibers: particle surface density in a cell for $w_0 = 0.1$, $w_0 = 1$, and $w_0 = 10$, for (a) $\mathrm{Re}_\ell = 10^{-2}$ and (b) $\mathrm{Re}_\ell = 10$.

Note that the Reynolds number affects this feature only by making the preferred region narrower. As the reference settling speed increases, the preferred region persists but moves from the vortices periphery to their center, while being still located in the downflow regions. This is consistent with the experimental results in Fig. 9. However, as $w_0 \geqslant 1$, a transition occurs from a narrow region to a broad sampling of the flow. In that case, the settling speed is too high for the particles to be significantly deviated by the flow and therefore fibers settle almost regardless of the vortices.

The next comparison focused on the orientation distribution of the fibers. Whereas all models predict similar particle preferential concentration at low inertia, only models accounting for inertial effects were able to capture correctly the orientation distribution, even for $\mathrm{Re}_\ell = 0.1$. Indeed, the peak at $\theta = 0$ corresponding to a horizontal fiber results mainly from inertia through Ω_1 [Eq. (13)]. As inertia increases, the peak around $\theta = 0$ becomes more important and the one at $\theta = \pm\pi/2$ vanishes; these two effects are well captured only by the full model M3. In order to go beyond the experimental case at $w_0 = O(1)$, Fig. 13 shows the role of w_0 on the orientation distribution, for $\mathrm{Re}_\ell = 1$. By comparison with the experimental results in Fig. 10 one can observe that w_0 plays a similar role as the Reynolds number Re_ℓ: at low reference settling velocity (or similarly Re_ℓ), the distribution is rather flat, with two peaks at $\theta = 0$ (horizontal fiber) and $\pm\pi/2$ (vertical fiber), whereas at larger w_0 (or Re_ℓ) the peaks at $\theta = \pm\pi/2$ vanish. In fact, considering the time-scale comparison of Eq. (16) one can see that the relative importance of the reorientation due to inertia depends similarly on Re_ℓ and w_0. As either of these two parameters increases, reorientation by inertia becomes faster, resulting in fibers oriented horizontally and thus settling in straight lines, as observed on the preferential trajectories in Fig. 12.

Finally we focused on the effective settling velocity through the vortical flow. At low inertia, the different models predicted correct settling rates, which is in fact consistent with Fig. 2(a), where all models predicted a similar 2D-averaged settling speed at low Reynolds number. At larger inertia however, only model M3 captures correctly the effective settling speed, while the other models significantly overestimate (inertialess models) or underestimate (low-inertia model) the effective settling velocity. The experimental data in Fig. 11 also show that the average settling speed diminishes as w_0 increases. This is further investigated in Fig. 14, showing the effective settling

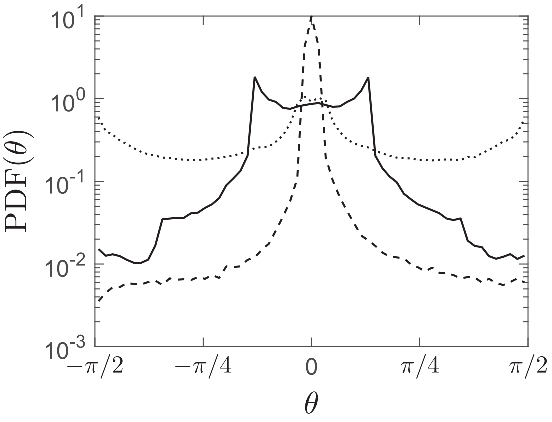

FIG. 13. Probability density function of the angle with the horizontal axis θ for three values of the reference settling velocity $w_0 = 0.1$ (dotted line), $w_0 = 1$ (solid line), and $w_0 = 10$ (dashed line), at $\mathrm{Re}_\ell = 1$.

velocity averaged over each periodic cell, normalized here by the 2D-averaged settling speed in a quiescent fluid $\langle W \rangle$. In two dimensions, the linearity of the settling speed with respect to gravity yields $\langle W \rangle = (W_\parallel + W_\perp)/2$. The curves obtained exhibit two behaviors, a significant decrease for $w_0 \leqslant 1$ and slow decrease at larger values of w_0, converging towards an effective settling velocity which corresponds to $W_\perp$. These two behaviors are related to the transition observed on preferential trajectories. At low w_0 fibers aggregate along downflow regions, and settling is therefore enhanced by the flow. Note that in this regime the dispersion is larger as trapping can occur more easily. This enhanced settling is reduced when w_0 increases, as trajectories tend to be located closer to the center of the vortices, where the vertical component of the flow is almost zero. Finally, at large values of the relative settling velocity, the ratio $V_z/\langle W \rangle$ takes almost a constant value equal to $W_\perp/\langle W \rangle$. Indeed, in this regime particles align horizontally and settle along straight vertical trajectories regardless of the flow. The flow effect is negligible as $U_0 \ll W_s$, and the resulting effective settling velocity tends towards the settling velocity in a quiescent fluid at finite inertia. Settling is therefore significantly enhanced by the vortices at low w_0, for particles that act almost as tracer particles, but at large w_0 the particles settling rate and trajectories are not affected by the flow.

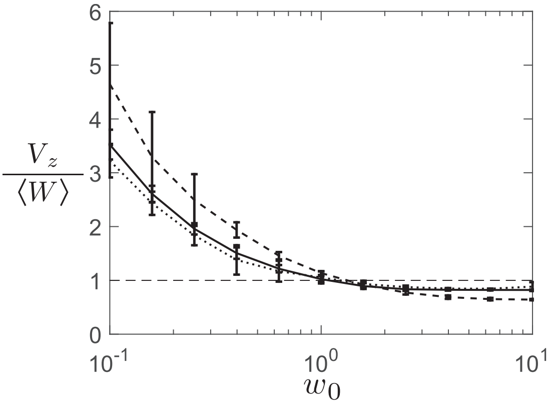

FIG. 14. Settling velocity V_z averaged over each periodic cell, normalized by the 2D averaged settling speed in a fluid at rest $\langle W \rangle$, as a function of w_0, for three values of the particle Reynolds number: $\mathrm{Re}_\ell = 0.1$ (dotted line), $\mathrm{Re}_\ell = 1$ (solid line), and $\mathrm{Re}_\ell = 10$ (dashed line).

To conclude, we performed a precise comparison of different theoretical models for inertial fibers settling in an external flow with well-controlled 2D experiments. Inertia was introduced here through a finite particle Reynolds number while keeping a low Stokes number. Whereas at low inertia preferential concentration and effective settling rates were correctly captured by all models, in particular the inertialess slender-body limit model, we showed that finite aspect ratio corrections and inertial corrections for $\mathrm{Re}_\ell \geqslant 1$ played a significant role on the trajectories, on preferential sampling and orientations, and on the effective settling velocity. The inertial corrections proposed in Ref. [25] were in very good agreement with the experimental data in all regimes, even at low particle aspect ratios, i.e. $A = O(10)$, and large particle Reynolds number, i.e., $\mathrm{Re}_\ell = O(10)$. Moreover, the pseudolinear formulation using a generalized mobility matrix that was introduced in this work provided excellent results while reducing considerably the computational cost. Using the general model (M3), we identified the key role played by the reference settling velocity $w_0 = W_s/U_0$ in describing the particles dynamics when settling is included in the problem.

The present work should provide guidance for choosing the appropriate modeling when the fiber aspect ratio is not extremely high or when the particle Reynolds number is not very small. In particular, it shows that the slender body limit model (denoted M0) should be used with care in these cases and that using models accounting for finite aspect ratio (M1) and finite inertia (M2 and M3) may be more sound.

ACKNOWLEDGMENTS

This work was undertaken under the auspices of ANR project “Collective Dynamics of Settling Particles in Turbulence” (ANR-12-BS09-0017-01), “Laboratoire d’Excellence Mécanique et Complexité” (ANR-11-LABX-0092), “Initiative d’Excellence” A*MIDEX (ANR-11-IDEX-0001-02), COST Action FP1005 “Fiber Suspension Flow Modeling,” and COST Action MP1305 “Flowing Matter.” We are greatly indebted to L. Bergougnoux for discussion and her help in experimental techniques. We also thank G. Bouchet, F. Candelier, and E. Climent for numerous discussions.

APPENDIX A: STOKES NUMBER EXPRESSION

The Stokes number compares the particle response time to the flow time scale, providing information on the relative importance of particle acceleration. Whereas for spherical particles characterized by a single length scale the Stokes number can be defined in an almost unique way, different definitions can be used for anisotropic particles. In this work we define the Stokes number in the same way as for spheres [19], starting from the particle advection equation (namely, Newton’s second law). Considering the low Reynolds number case, the particle advection equation can be expressed as

$$m_p \frac{dV_i}{dT} = (m_p - m_f)\mathbf{g}\cdot\mathbf{e}_i - R_{ij}(V_j - U_j), \tag{A1}$$

using Einstein’s summation convention. Here m_p and m_f are the particle and corresponding fluid mass, $\mathbf{V}$ is the particle velocity and V_i its components, T the time, $\mathbf{g}$ the gravitational acceleration, $\mathbf{U}$ the fluid velocity, and R_{ij} the resistance matrix components, giving the fluid drag force as a linear function of the relative velocity in the low Reynolds number case. Introducing the mobility matrix M_{ij} so that $M_{ij}R_{jk} = \delta_{ik}$ and using the flow scales as reference scales, the nondimensional advection equation reads

$$m_p\dot{\gamma} M_{ij}\frac{dv_j}{dt} = w_i - v_i + u_i, \tag{A2}$$

where lower case letters denote nondimensional quantities, and $\mathbf{w}$ is the settling speed in a quiescent fluid.

For spheres the isotropic mobility matrix allows one to define the Stokes number St from the dimensionless coefficient scaling the acceleration, $m_p\dot{\gamma}M_{ij} = \mathrm{St}\,\delta_{ij}$. A cylindrical rod is characterized by two mobility coefficients, $M_{\parallel} = (4\pi\mu\ell\epsilon)^{-1}$ along the principal axis and $M_{\perp} = (8\pi\mu\ell\epsilon)^{-1}$ in the two normal directions [22]. Following a similar approach one can define the Stokes number for a cylindrical rod considering a spherically averaged mobility, in a similar way as in Ref. [20] for ellipsoids, resulting in

$$\mathrm{St} = m_p\dot{\gamma}\frac{M_{\parallel} + 2M_{\perp}}{3} = \frac{1}{3}\frac{a^2\rho_p\dot{\gamma}}{\mu\epsilon}. \tag{A3}$$

As shown throughout the paper, corrections to the mobility coefficients in the presence of inertia do not significantly affect the typical scaling, so that this definition of the Stokes number obtained at zero Reynolds number remains valid at finite Reynolds number.

APPENDIX B: EXPRESSIONS OF THE G_y AND G_z AND $\tilde{\omega}$ FUNCTIONS FOR THE DIFFERENT MODELS

The dynamics of a settling fiber in a cellular flow is modeled by Eqs. (17) and (18). The functions G_y and G_z and $\tilde{\omega}$ depend on the different models and read in the general case

$$G_y(\epsilon,\mathrm{Re}_\ell) = 1 + (F_\perp - 2F_\parallel)\epsilon, \tag{B1}$$

$$G_z(\epsilon,\mathrm{Re}_\ell,\theta) = 1 + \frac{(F_\perp - 2F_\parallel)\sin^2\theta - F_\perp}{1+\sin^2\theta}\epsilon, \tag{B2}$$

$$\tilde{\omega}(w,\lambda,\alpha,\epsilon,\mathrm{Re}_\ell) = -\frac{3}{4}\frac{w}{\lambda}F_G(\mathrm{Re}_\ell,\alpha)\epsilon. \tag{B3}$$

These expressions can be simplified according to the model considered.

Model 0:

$$G_y = 1, \quad G_z = 1, \quad \tilde{\omega} = 0. \tag{B4}$$

Model 1:

$$G_y = 1 + \left(\ln 4 - \frac{5}{2}\right)\epsilon, \quad G_z = 1 + \left[\ln 4 - \frac{1+5\sin^2\theta}{2(1+\sin^2\theta)}\right]\epsilon, \quad \tilde{\omega} = 0. \tag{B5}$$

Model 2:

$$G_y = 1 + \left(\ln 4 - \frac{5}{2}\right)\epsilon, \tag{B6}$$

$$G_z = 1 + \left[\ln 4 - \frac{1+5\sin^2\theta + \mathrm{Re}_\ell}{2(1+\sin^2\theta)}\right]\epsilon, \tag{B7}$$

$$\tilde{\omega} = \frac{5}{16}\frac{w}{\lambda}\sin(2\alpha)\,\mathrm{Re}_\ell\,\epsilon. \tag{B8}$$

Model 3: These functions are given by Eqs. (B1)–(B3), with

$$F_\parallel = \frac{1}{2}\left[\frac{E_1(2\mathrm{Re}_\ell) + \ln(2\mathrm{Re}_\ell) - e^{-2\mathrm{Re}_\ell} + \gamma + 1}{2\mathrm{Re}_\ell} + E_1(2\mathrm{Re}_\ell) + \ln(\mathrm{Re}_\ell) + \gamma - 3\ln 2 + 1\right],$$

$$F_\perp = E_1(\mathrm{Re}_\ell) + \ln(\mathrm{Re}_\ell) - \frac{e^{-\mathrm{Re}_\ell} - 1}{\mathrm{Re}_\ell} + \gamma - \frac{1}{2} - \ln 4, \tag{B9}$$

and

$$F_G = \left(\frac{1}{2\mathrm{Re}_\ell(1-c_\alpha)}\left\{2+2\frac{e^{-\mathrm{Re}_\ell(1-c_\alpha)}-1}{\mathrm{Re}_\ell(1-c_\alpha)} - E_1[\mathrm{Re}_\ell(1-c_\alpha)] - \ln[\mathrm{Re}_\ell(1-c_\alpha)] - \gamma\right\}\right.$$
$$+\frac{1}{2\mathrm{Re}_\ell(1+c_\alpha)}\left\{2+2\frac{e^{-\mathrm{Re}_\ell(1+c_\alpha)}-1}{\mathrm{Re}_\ell(1+c_\alpha)} - E_1[\mathrm{Re}_\ell(1+c_\alpha)] - \ln[\mathrm{Re}_\ell(1+c_\alpha)] - \gamma\right\}$$
$$\left.-\frac{1}{\mathrm{Re}_\ell(1-c_\alpha)c_\alpha}\left[1-\frac{1-e^{-\mathrm{Re}_\ell(1-c_\alpha)}}{\mathrm{Re}_\ell(1-c_\alpha)}\right] + \frac{1}{\mathrm{Re}_\ell(1+c_\alpha)c_\alpha}\left[1-\frac{1-e^{-\mathrm{Re}_\ell(1+c_\alpha)}}{\mathrm{Re}_\ell(1+c_\alpha)}\right]\right)\sin(2\alpha), \tag{B10}$$

noting $c_\alpha = \cos\alpha$, where γ is Euler constant and E_1 is the exponential integral function,

$$E_1(x) = \int_x^\infty \frac{e^{-t}}{t}\,dt. \tag{B11}$$

[1] G. A. Voth and A. Soldati, Anisotropic particles in turbulence, Annu. Rev. Fluid Mech. **49**, 249 (2017).
[2] S. Parsa, J. S. Guasto, M. Kishore, N. T. Ouellette, J. P. Gollub, and G. A. Voth, Rotation and alignment of rods in two-dimensional chaotic flow, Phys. Fluids **23**, 043302 (2011).
[3] S. Parsa, E. Calzavarini, F. Toschi, and G. A. Voth, Rotation Rate of Rods in Turbulent Fluid Flow, Phys. Rev. Lett. **109**, 134501 (2012).
[4] G. B. Jeffery, The motion of ellipsoidal particles immersed in a viscous fluid, Proc. R. Soc. London A **102**, 161 (1922).
[5] M. Shin and D. L. Koch, Rotational and translational dispersion of fibres in isotropic turbulent flows, J. Fluid Mech. **540**, 143 (2005).
[6] A. Pumir and M. Wilkinson, Orientation statistics of small particles in turbulence, New J. Phys. **13**, 093030 (2011).
[7] R. Ni, N. T. Ouellette, and G. A. Voth, Alignment of vorticity and rods with Lagrangian fluid stretching in turbulence, J. Fluid Mech. **743**, R3 (2014).
[8] H. Zhang, G. Ahmadi, F.-G. Fan, and J. B. McLaughlin, Ellipsoidal particles transport and deposition in turbulent channel flows, Int. J. Multiphase Flow **27**, 971 (2001).
[9] C. Marchioli, M. Fantoni, and A. Soldati, Orientation, distribution, and deposition of elongated, inertial fibers in turbulent channel flow, Phys. Fluids **22**, 033301 (2010).
[10] L. Zhao, N. R. Challabotla, H. I. Andersson, and E. A. Variano, Rotation of Nonspherical Particles in Turbulent Channel Flow, Phys. Rev. Lett. **115**, 244501 (2015).
[11] L.-P. Wang and M. R. Maxey, Settling velocity and concentration distribution of heavy particles in homogeneous isotropic turbulence, J. Fluid Mech. **256**, 27 (1993).
[12] C. Y. Yang and U. Lei, The role of the turbulent scales in the settling velocity of heavy particles in homogeneous isotropic turbulence, J. Fluid Mech. **371**, 179 (1998).
[13] T. Bosse, L. Kleiser, and E. Meiburg, Small particles in homogeneous turbulence: Settling velocity enhancement by two-way coupling, Phys. Fluids **18**, 027102 (2006).
[14] H. Stommel, Trajectories of small bodies sinking slowly through convection cells, J. Mar. Res. **8**, 24 (1949).
[15] M. R. Maxey and J. J. Riley, Equation of motion for a small rigid sphere in a nonuniform flow, Phys. Fluids **26**, 883 (1983).
[16] M. R. Maxey, The motion of small spherical particles in a cellular flow field, Phys. Fluids **30**, 1915 (1987).
[17] F. Toschi and E. Bodenschatz, Lagrangian properties of particles in turbulence, Annu. Rev. Fluid Mech. **41**, 375 (2009).

[18] S. Balachandar and J. K. Eaton, Turbulent dispersed multiphase flow, Annu. Rev. Fluid Mech. **42**, 111 (2010).

[19] L. Bergougnoux, G. Bouchet, D. Lopez, and E. Guazzelli, The motion of solid spherical particles falling in a cellular flow field at low Stokes number, Phys. Fluids **26**, 093302 (2014).

[20] R. Mallier and M. Maxey, The settling of nonspherical particles in a cellular flow field, Phys. Fluids **3**, 1481 (1991).

[21] C. Siewert, R. P. J. Kunnen, M. Meinke, and W. Schröder, Orientation statistics and settling velocity of ellipsoids in decaying turbulence, Atmos. Res. **142**, 45 (2014).

[22] G. K. Batchelor, Slender-body theory for particles of arbitrary cross-section in Stokes flow, J. Fluid Mech. **44**, 419 (1970).

[23] A. J. Heymsfield, C. Schmitt, and A. Bansemer, Ice cloud particle size distributions and pressure-dependent terminal velocities from in situ observations at temperatures from 0° to -86° C, J. Atmos. Sci. **70**, 4123 (2013).

[24] R. G. Cox, The motion of long slender bodies in a viscous fluid. Part 1. General theory, J. Fluid Mech. **44**, 791 (1970).

[25] R. E. Khayat and R. G. Cox, Inertia effects on the motion of long slender bodies, J. Fluid Mech. **209**, 435 (1989).

[26] F. P. Bretherton, The motion of rigid particles in a shear flow at low Reynolds number, J. Fluid Mech. **14**, 284 (1962).

[27] L. G. Leal and E. J. Hinch, The rheology of a suspension of nearly spherical particles subject to Brownian rotations, J. Fluid Mech. **55**, 745 (1972).

[28] S. G. Mason and R. St J. Manley, Particle motions in sheared suspensions: Orientations and interactions of rigid rods, Proc. R. Soc. London A **238**, 117 (1956).

[29] E. Guazzelli and J. F. Morris, *A Physical Introduction to Suspension Dynamics* (Cambridge University Press, Cambridge, 2011), Vol. 45.

[30] S. Kim and S. J. Karrila, *Microhydrodynamics: Principles and Selected Applications* (Dover, New York, 1991).

[31] G. Subramanian and D. L. Koch, Inertial effects on fibre motion in simple shear flow, J. Fluid Mech. **535**, 383 (2005).

[32] J. Einarsson, F. Candelier, F. Lundell, J. R. Angilella, and B. Mehlig, Effect of weak fluid inertia upon Jeffery orbits, Phys. Rev. E **91**, 041002 (2015).

[33] P. Meunier and T. Leweke, Analysis and treatment of errors due to high velocity gradients in particle image velocimetry, Exp. Fluids **35**, 408 (2003).